



Supplement of

Regional variability of aerosol impacts on clouds and radiation in global kilometer-scale simulations

Ross J. Herbert et al.

Correspondence to: Ross J. Herbert (r.j.herbert@leeds.ac.uk)

The copyright of individual parts of the supplement might differ from the article licence.

S1 The aerosol perturbation

Figure S1 shows the simulated aerosol extinction fields in our simulations. The pre-industrial aerosol is representative of the natural background aerosol and is taken from the aerosol climatology MACv2.0 (Kinne, 2019). The present-day aerosol distribution includes a representation of anthropogenic aerosol emissions that are simulated using the MACv2-SP plume model (Stevens et al., 2017). The aerosol perturbation (Δ AOD) from MACv2-SP is shown on the right of Fig. S1.

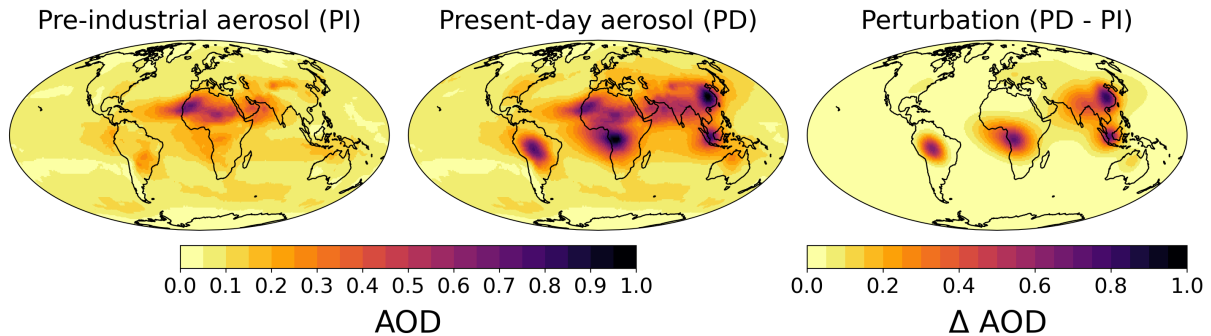


Figure S1. Spatial distribution of aerosol optical depth (AOD) in the pre-industrial (PI; left) and present-day (PD; middle) simulations. The change in AOD between the two simulations (PD-PI) is shown on the right.

S2 Testing the temporal decomposition method

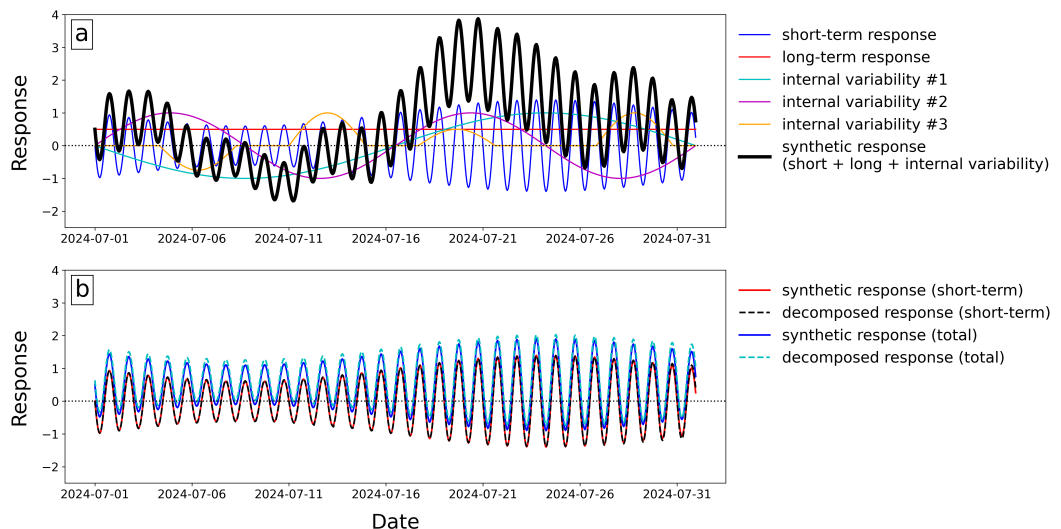


Figure S2. Figure demonstrating the decomposition method. A synthetic response in (a) includes a short-term diurnal component with a time-dependent amplitude, a long-term persistent time-independent component, and internal variability from multiple sources. The aim of the decomposition method is to sufficiently isolate any underlying short-term response along with a persistent response. The result of the decomposition method from the manuscript applied to the synthetic response (short-term + long-term + internal variability[1-3]) is shown in (b).

Figure S2 demonstrates the ability of the temporal decomposition method to isolate short-term (diurnal) and long-term (persistent) responses amid internal variability. Multiple sources of synthetic internal variability / noise are added to a diurnal response with day-to-day variability in amplitude and a persistent (time-independent) response. This is shown in Fig. S2a. Our method aims to isolate the responses from the internal variability. Figure S2b shows the result of applying the decomposition method (Sect. 2.4). The method successfully isolates the responses. The total decomposed response is slightly higher than the synthetic response due to an imbalance in the synthetic internal variability from the third source. This demonstrates a weakness in the method when internal variability is strongly weighted towards a single direction of response (positive/ negative).

S3 Global-scale analysis: additional figures

This section includes two additional figures related to Sect. 3.1 in the manuscript. The temporal decomposition method (Sect. 2.4) is used to analyze the global regional-scale responses of condensate mass flux at 500 hPa (M_{flux} , Fig. S3) and ice water path (IWP, Fig. S4) due to anthropogenic aerosol. The decomposition is performed on data regredded to a global 15° grid using the Climate Data Operators (CDO; <http://www.idris.fr/media/ada/cdo.pdf>) software operator gencon which generates first order conservative remapping weights. The weights are applied to every output timestep.

500 hPa M_{flux} response (PD - PI)

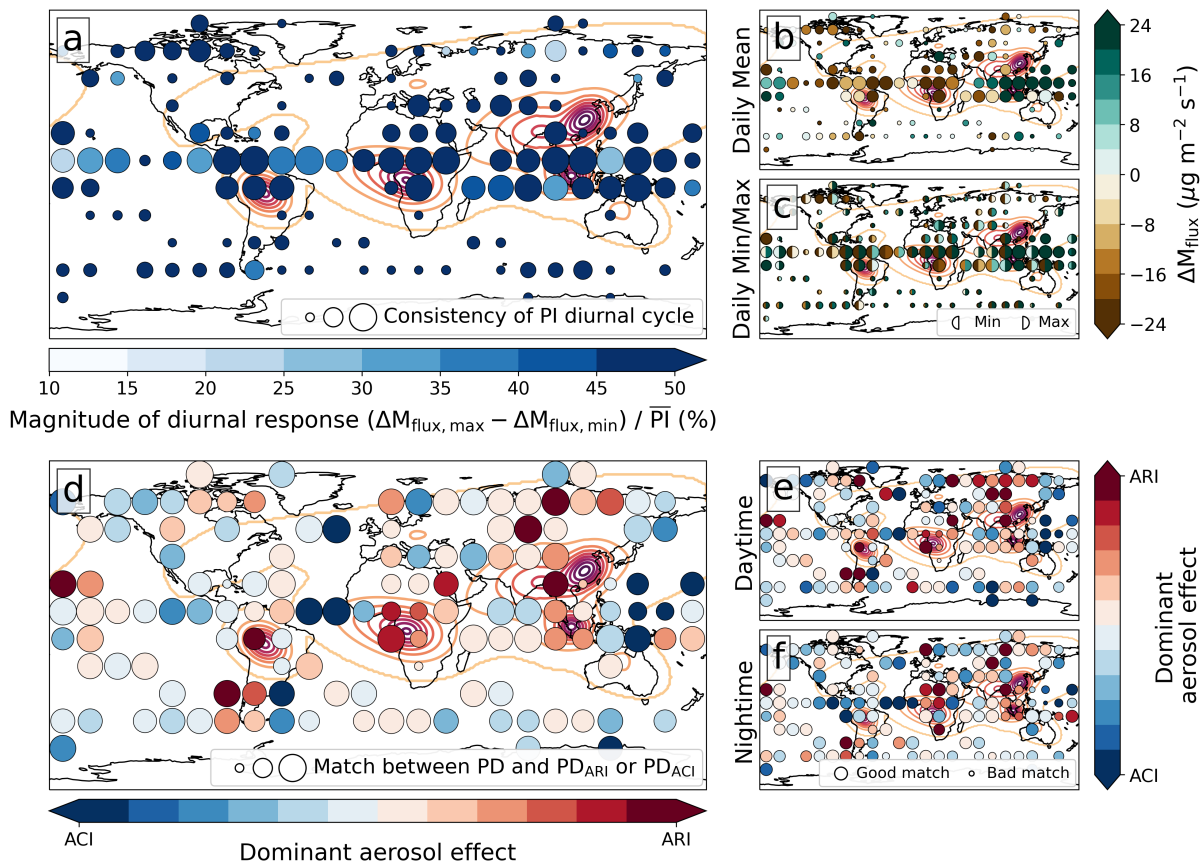


Figure S3. Mean diurnal response of condensate mass flux (M_{flux}) at 500 hPa to the aerosol perturbation (PD - PI) from each $15^\circ \times 15^\circ$ region. Panels **a – c** show the diurnal magnitude of the response as a percentage (**a**), absolute daily mean (**b**), and absolute daily minimum/maximum (**c**). A larger circle size in **a – c** represents a location with an increasingly consistent diurnal cycle throughout the PI simulation. Panels **d – f** show the dominating aerosol effect (ARI/ACI) driving the LWP response during the diurnal cycle (**d**), day (**e**), and night (**f**). A larger circle size in **d – f** represents a better match between the individual response (PD_{ARI} or PD_{ACI}) and total response (PD). All panels show the AOD perturbation as contour lines at 0.05 increments.

Ice Water Path response (PD - PI)

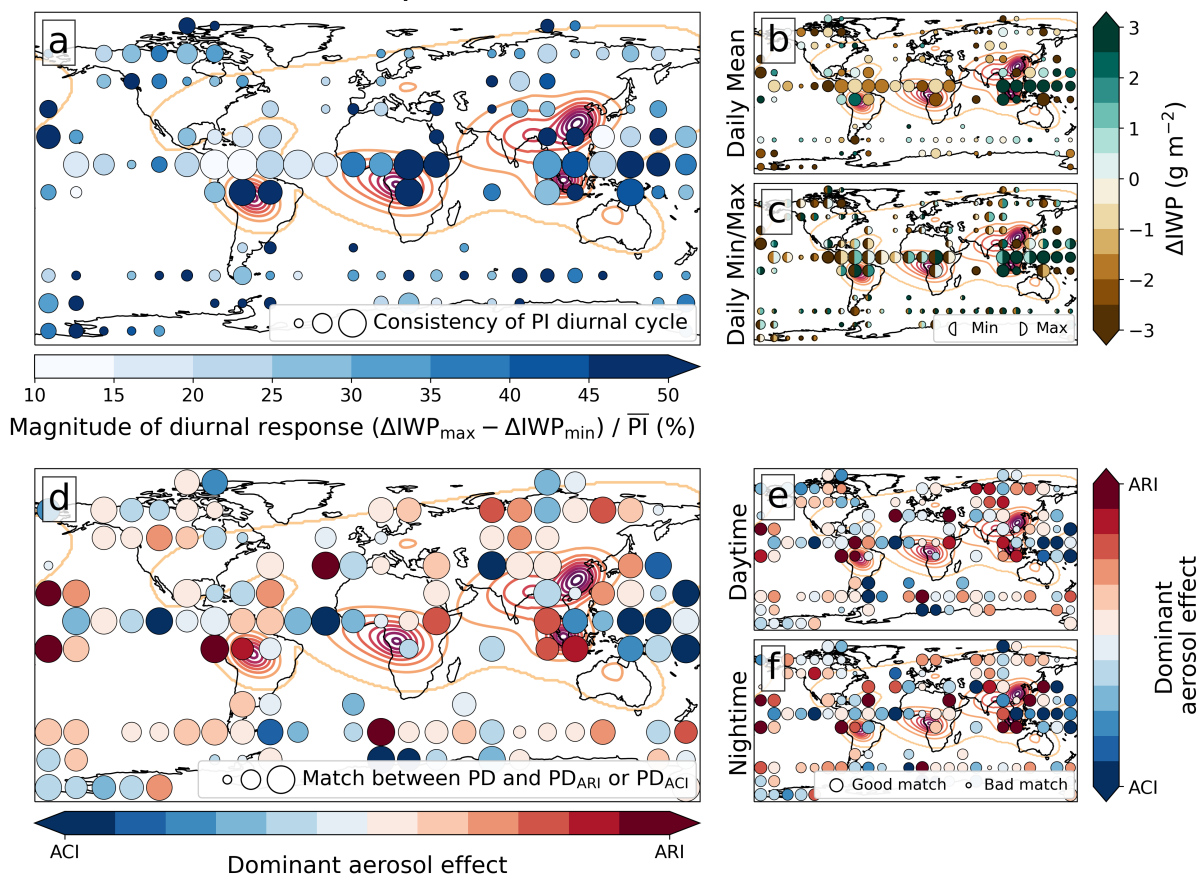


Figure S4. Same as Fig. S3 but showing the column integrated ice water path (IWP).

S4 Regional-scale analysis: additional figures

This section includes additional figures related to Sect. 3.2. Figures S5 and S6 show the regional diurnal responses of liquid cloud cover (CF_{liquid}) and surface flux of latent heat (LHF) for all six regions shown in Fig. 9. Figure S7 shows the diurnal response of precipitation in the three convective regions (The Congo, The Amazon, and the Maritime Continent) shown in Fig. 9. The response is shown for all gridpoints, and those that have ascending air at 500hPa indicating convection. The responses are normalised to the total number of grid points inside the region. The responses in the Congo and the Amazon are of the same magnitude indicating that the regional-mean precipitation response is occurring primarily in ascending regions and likely associated with convection. The Maritime Continent shows that the diurnal cycle of the precipitation response is associated with convection, but there is an additional time-independent increase due to the larger-scale environment. Figure S8 shows the distribution of precipitation rates (P) across each convective region using the 5-km resolution output. ARI and ACI impact precipitation across all intensities (Fig. S8a – c) but the biggest impact to the total precipitation occurs at precipitation rates above 10 mm hr⁻¹ (Fig. S8g – i), which are magnitudes associated with deeper convection rather than shallow convection. Figures S9 to S11 show regional-mean responses of cloud properties and thermodynamic profiles (as in Figs. 11 – 13) in the three non-convective regions (East Asia, Northwest Pacific Ocean, and Southeast Atlantic Ocean).

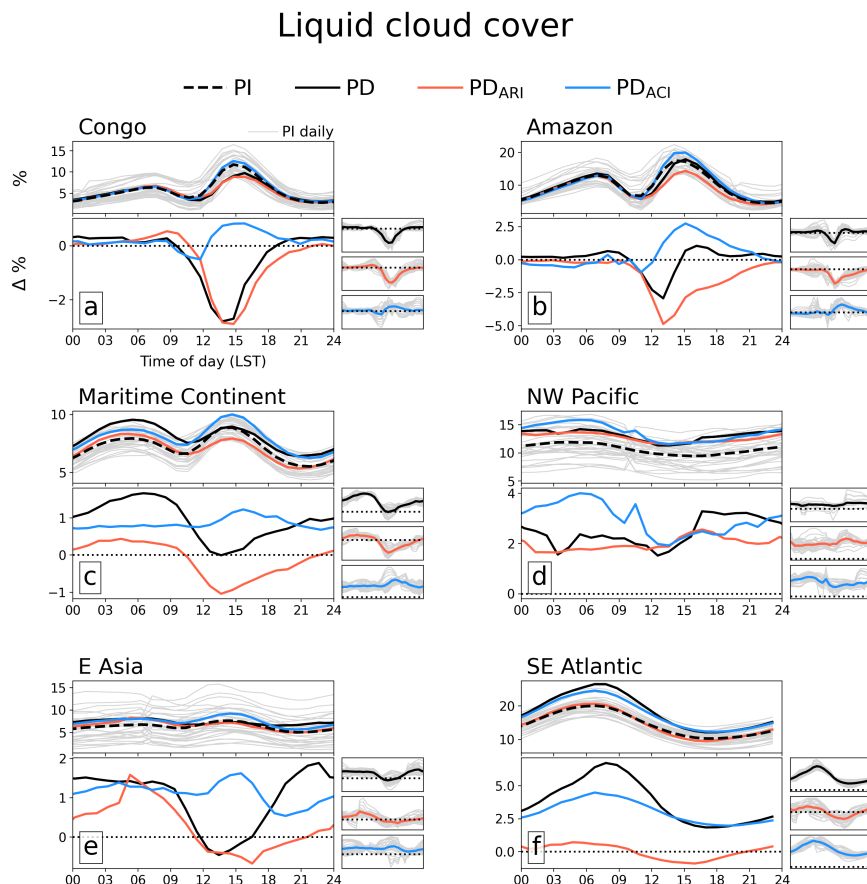


Figure S5. Composites of decomposed diurnal response of liquid cloud fraction (CF_{liquid}) over the six regions of interest. For each region (a – f) the top sub-plot shows the mean diurnal cycle of CF_{liquid} (%) in each simulation, with grey lines showing each day of the PI simulation. The lower sub-plots show the PD response ($\Delta \%$) to aerosol perturbations in each simulation ($PDx - PI$), which are repeated individually to the right along with grey lines showing each day of the composite.

Latent heat flux

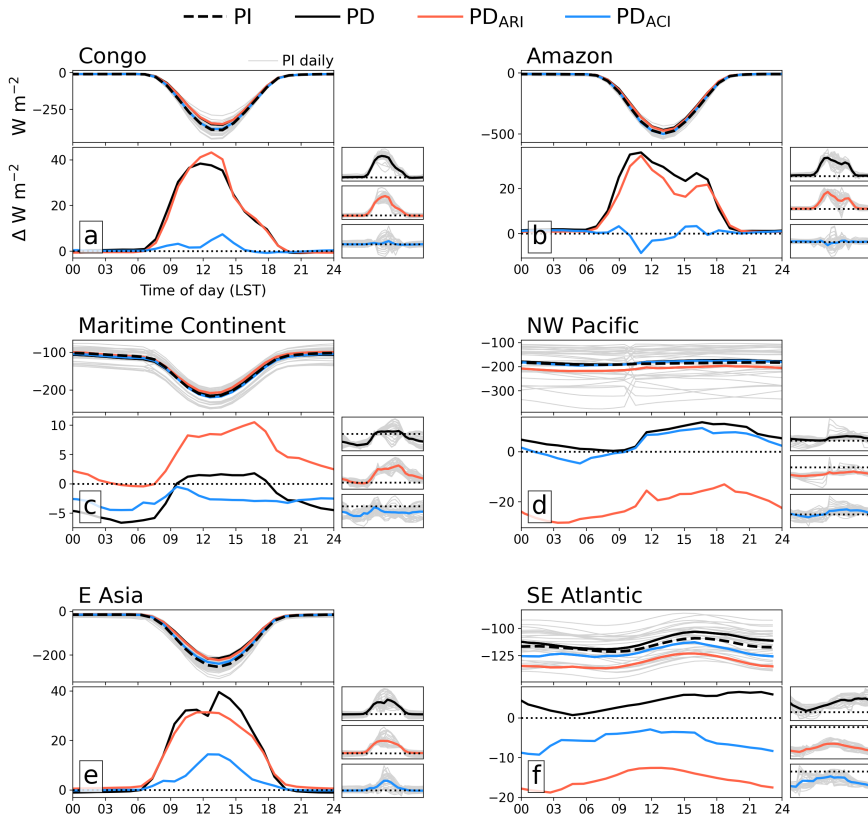


Figure S6. Same as Fig. S5 but showing the response of surface flux of latent heat (LHF). Negative values respond to a loss of energy from the surface to the atmosphere in the form of evaporation.

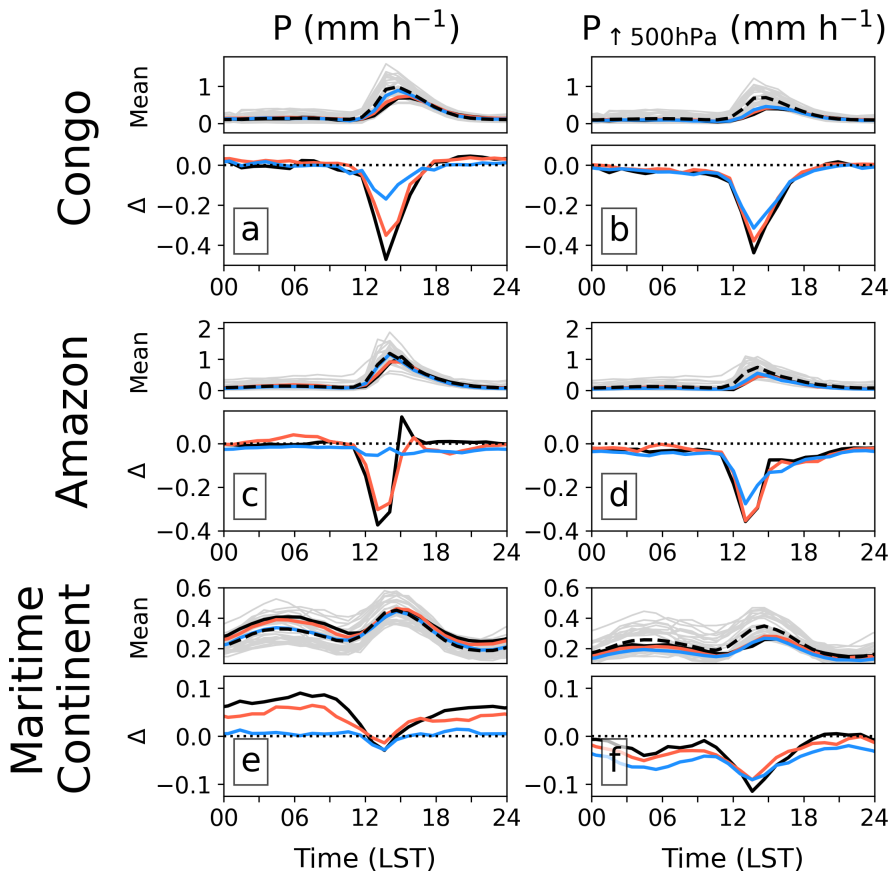


Figure S7. Composites of decomposed diurnal response of precipitation over the three convective regions for all grids (a, c, e) and for those with ascending air at 500 hPa (b, d, f). Data has been regredded onto a 1° grid. For each region the top sub-plot shows the mean diurnal cycle of P (mm h^{-1}) in each simulation, with grey lines showing each day of the PI simulation. The lower sub-plots show the PD response (Δ mm h^{-1}) to aerosol perturbations in each simulation ($\text{PD}_X - \text{PI}$), which are repeated individually to the right along with grey lines showing each day of the composite.

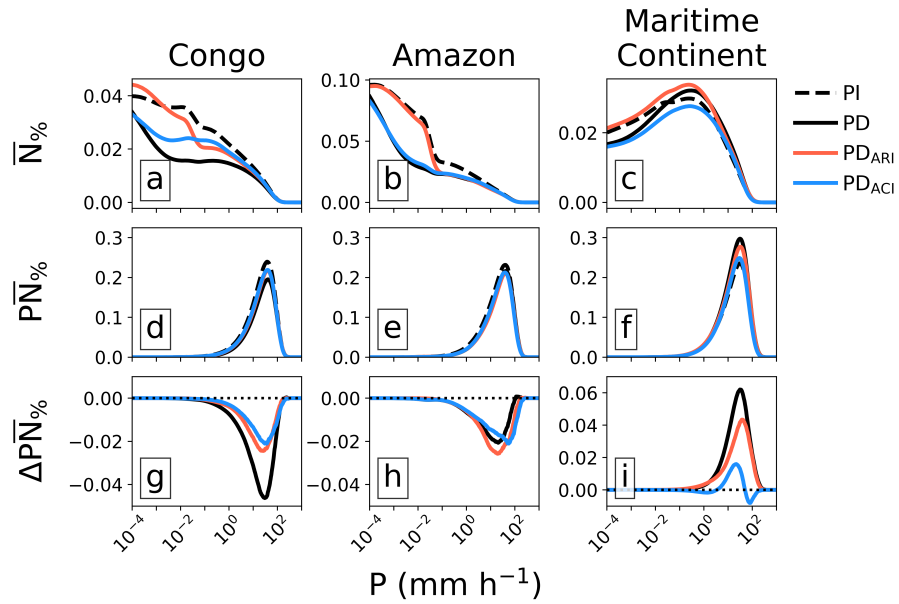


Figure S8. Distribution of time series mean precipitation rates in each of the three convective regions. Rows show the percentage of grid cells ($\bar{N}\%$) in each bin $\text{dlog}_{10}P$ (a – c), the total precipitation rate ($P\bar{N}\%$) per bin (d – f), and the change in total precipitation rate ($\Delta P\bar{N}\%$) per bin (g – i). Total precipitation rates ($P\bar{N}\%$ and $\Delta P\bar{N}\%$) for the Congo and Amazon are shown on the same scale to aid comparison.

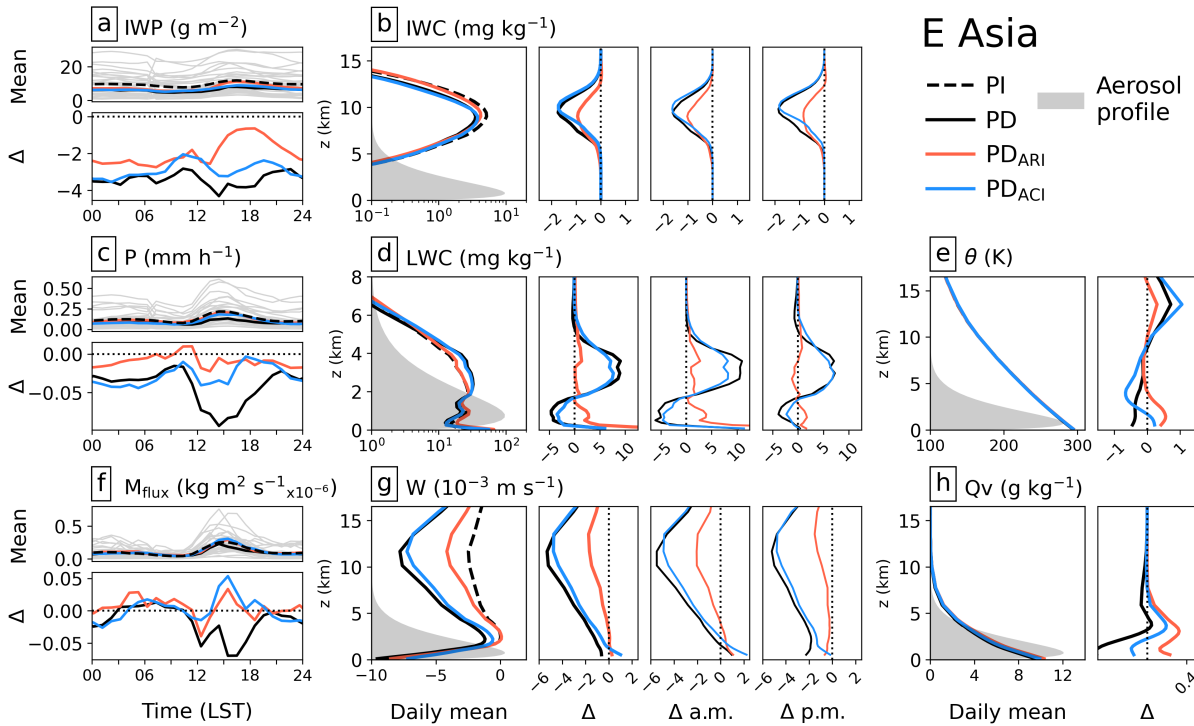


Figure S9. Composites showing the regional-mean change in cloud and thermodynamic properties in the East Asia region. Diurnal composites (a, c, f) show mean diurnal cycles of IWP (a), precipitation rate (c), and M_{flux} (f) in the top sub-panel, and the response of each variable to the aerosol perturbation in the lower sub-panel ($\text{PD}_X - \text{PI}$). Mean vertical profiles are shown for IWC (b), LWC (d), potential temperature θ (e), vertical velocity W (g), and water vapor Qv (h). Profiles for each variable include the mean from each simulation on the left and diurnal-mean changes due to the aerosol perturbation on the right ($\text{PD}_X - \text{PI}$). Plots b, d, and g also show the diurnal-mean change separated into contributions from the a.m. (00:00 to 12:00 LST) and p.m. (12:00 - 24:00 LST). Profiles of the aerosol perturbation are shown in grey alongside the mean profiles. Note that the LWC is shown from 0 to 8 km and all other profiles are shown from 0 to 16 km.

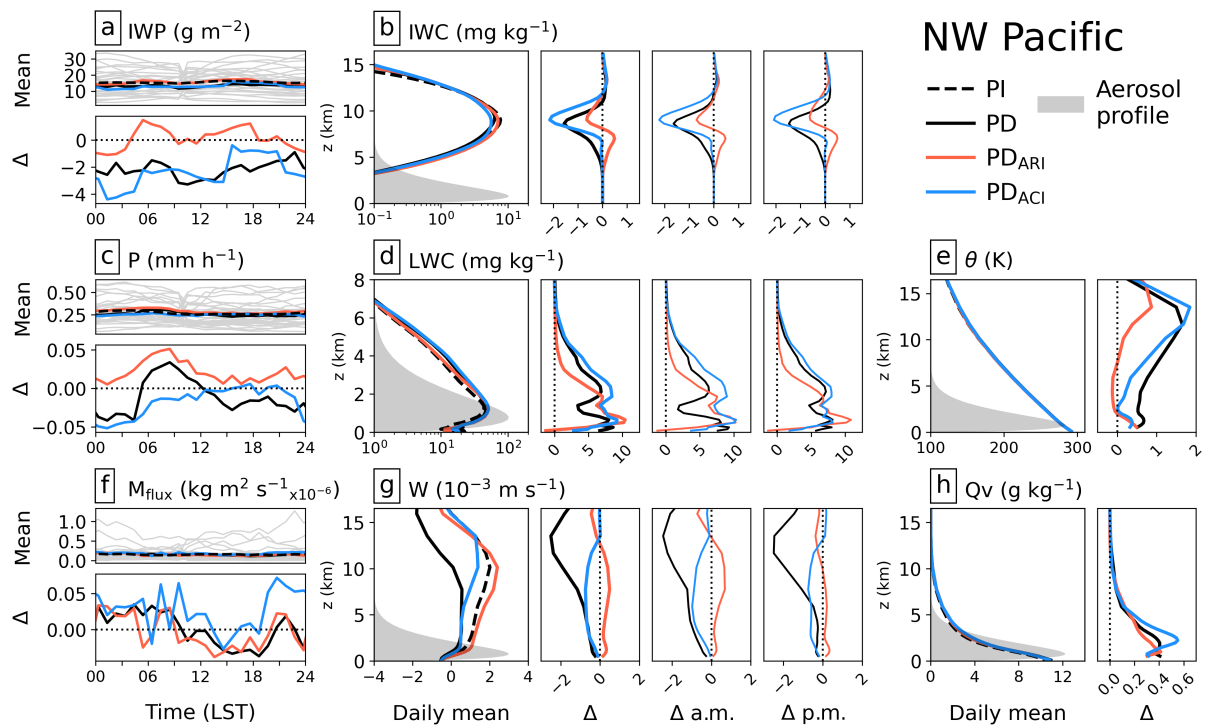


Figure S10. Same as Fig. S9 but for the Northwest Pacific Ocean region.

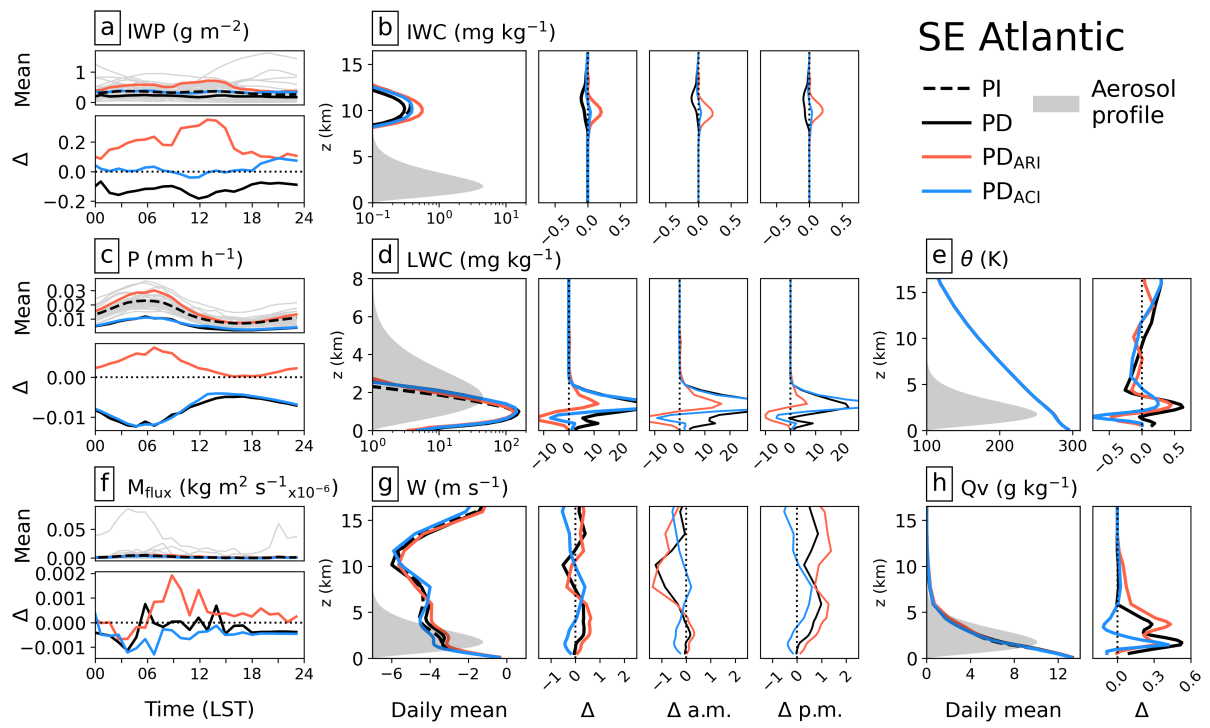


Figure S11. Same as Fig. S9 but for the Southeast Atlantic Ocean region.

References

- Kinne, S.: Aerosol radiative effects with MACv2, *Atmospheric Chemistry and Physics*, 19, 10 919–10 959, <https://doi.org/10.5194/acp-19-10919-2019>, publisher: Copernicus GmbH, 2019.
- Stevens, B., Fiedler, S., Kinne, S., Peters, K., Rast, S., Mösse, J., Smith, S. J., and Mauritsen, T.: MACv2-SP: a parameterization of anthropogenic aerosol optical properties and an associated Twomey effect for use in CMIP6, *Geoscientific Model Development*, 10, 433–452, <https://doi.org/10.5194/gmd-10-433-2017>, publisher: Copernicus GmbH, 2017.